Cu2+-labeled, SPION loaded porous silica nonparticles for cell labeling and multifunctional imaging probes

Patel, Daksha; Kell, Arnold; Simard, Benoit; Deng, Jixian; Xiang, Bo; Lin, Hung-Yu; Gruwel, Marco; Tian, Ganghong

Publisher's version / Version de l'éditeur:
https://doi.org/10.1016/j.biomaterials.2009.12.025
Biomaterials, 31, 10, pp. 2866-2873, 2010-01-06

Cu^{2+}-labeled, SPION loaded porous silica nanoparticles for cell labeling and multifunctional imaging probes

Patel Daksha; Kell Arnold; Simard Benoit;Deng Jixian; Xiang Bo; Lin Hung-Yu; Gruwel Marco; Tian Ganghong

Abstract

We have developed an ion-sensing nanoparticle that is comprised of a superparamagnetic iron oxide (SPIO) core encapsulated with a porous silica shell. The latter can be readily anchored with ligands capable of coordinating with positron-emitting metal. Evidently, this nanoparticle has a great potential for use in cell tracking with magnetic resonance (MR) imaging and positron emission tomography (PET). Herein we report the synthesis, surface functionalization and characterization of the magnetic nanoparticle-based probes and evaluate their cell-labeling efficacy, cytoxicity and relaxivity in comparison to one of the most commonly utilized MRI contrast agents, Feridex®.

Keywords: Cell viability; Copper; Cytotoxicity; In vitro test; MRI (magnetic resonance imaging); Surface modification

1. Introduction

The precise visualization of an organ or a lesion is important for understanding its biological activity, accurate diagnosis and treatment of the diseases [1]. Although some of the imaging modalities currently available can provide adequate images, most of them have inherent limitations, including low sensitivity and insufficient spatial or temporal resolution [2], [3] and [4]. For example, the sensitivity of magnetic resonance imaging (MRI) is often found insufficient for detection of tissue injury, assessment of tissue/organ function and more recently for tracking of the implanted stem cells. As a result, a variety of approaches are currently being developed to overcome the limited sensitivity of the current MRI techniques. Cheon and coworkers have developed impressive $MnFe_2O_3$-based nanopaticles that have magnetic properties far superior to those of the currently available MRI probes, reflected by enhanced T_2 values [5]. Another approach that has recently been given attention by the chemistry community is tuning the surface chemistry of a nanoparticle to improve the intracellular loading of the MRI probes into cells of interest [6]. The development of surface modified nanoparticle-based probes is also intriguing because the surface of the NP's can allow the introduction of an additional imaging modality such as positron emission tomography (PET). It is possible to get good quality images in clinic by combining two imaging modalities, such as MRI and PET [7], [8], [9] and [10]. In order to avail all the advantages of the two imaging modalities, development of a sensitive probe that can be detected by both the imaging modalities would be very useful clinically.

A critical feature for any potential MRI/PET contrast agent is that it must be non-toxic. There are numerous examples in the literature that show silica to fit into this criteria. As such, we have developed a series of nanoparticle probes consisting of an iron oxide core as the MRI probe, a

porous silica shell to impart biocompatibility and modified the surface of these nanoparticles with a ligand capable of coordinating with metal ions of interest for PET imaging, namely ^{64}Cu and ^{111}In [11]. We have chosen to utilize a porous silica shell because the MRI contrast enhancement imparted by the nanoparticles requires that there should be intimate contact between water molecules and the iron oxide nanoparticle. The pores in the silica shell should provide such an opportunity. We have also tuned the synthesis of the nanoparticles such that we can controllably incorporate either single iron oxide nanoparticle into a silica shell or a cluster of the nanoparticles into the silica matrix. The latter is of particular interest because it has recently been reported that clustering of superparamagnetic magnetite nanocrystals results in higher saturation magnetization than that of the individual nanoparticles [12]. This can be attributed to the interaction between the assembled nanocrystals. Further, it was also proposed that clustering of monodisperse SPIO particles inside the micelles resulted in high local concentrations or loadings of SPIOs in each nanoparticle that can consequently increase the relaxivity r_2 values *i.e.*, the ability to shorten spin–spin relaxation time of protons [13]. Though it has not been determined if the silica coated analogs will behave in a similar fashion.

In this study we have developed surface functionalized SPIO@SiO_2 nanoparticles that can provide MRI contrast comparable to commercially available Feridex®. This report also describes how the SPIO loading within the silica matrix affects the overall nanoparticle relaxivity. In addition, we have developed a unique ligand that allows us to elucidate how tuning of the surface charge on the resulting SPIO@SiO_2 influences endocytosis of the nanoparticles into mesenchymal stem cells and the effect of the resulting nanoparticle uptake into the stem cells on the cell viability.

2. Experimental procedures

2.1. Materials

The reagents and solvents were obtained from the commercial sources: iron(II) chloride tetrahydrate (99%), iron(III) chloride hexahydrate (97%), diethylene glycol (99%), sodium hydroxide (97%; 20–40 mesh beads), Cetyltrimethylammonium bromide (CTAB), tetraethyl orthosilicate (TEOS), pyridine, Ethylenetriaminetetraacetic acid dianhydride (EDTA-bis(anhydride)) and aqueous ammonia were purchased from Aldrich and used without further purification. 3-Aminopropyl triethoxysilane (APTES), *N*-(Trimethoxysilyl)propyl-*N*,*N*,*N*-trimethylammonium chloride (50% in methanol) were purchased from Gelest. The fatty acid-capped iron oxide nanocrystal was obtained from Ferrotec Inc. All the chemicals and solvents were of reagent grade and used without further purification. Magnetite nanoparticles were prepared as describe previously [14]. X-ray diffractometry (XRD) measurements were performed with a Bruker AXS X-ray system equipped with a graphite monochromator (Cu Kα radiation, λ 1.54056 Å). A transmission electron microscope (TEM) Philips CM20 FEG operating at 200 kV was used to determine particle size and morphology. NMR studies were performed on a Varian Gemini-300 spectrometer. FT-IR spectra were obtained on a Perkin–Elmer 1600 spectrometer using KBr pellets. XPS spectrum for Cu was recorded on Physical Electronics 5600 multi-technique system. UV–visible spectra recorded on a Cary 5000 instrument. Zeta potentials of the silica nanoparticles were obtained with a Zetasizer 2000 (Malvern Instruments Ltd., U.K.). Measurements were performed at 25 °C and various pH using

a 1000 Hz modulator frequency and a cell drive voltage of 120 V. The values reported are the averages of three measurements.

The synthesis of the silica coated nanoparticles and the change of their surface charges following the surface modifications and subsequent coordination with Cu^{2+} ions are shown in (Scheme 1).

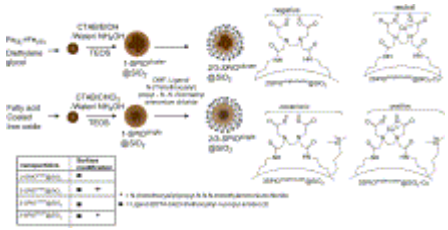

Scheme 1.

2.2. Synthesis of single SPIO in the silica matrix (1-SPIO^{single}@SiO_2)

A dispersion of the oleate-capped iron oxide nanocrystals (NCs) (0.1 g) in chloroform (20.0 mL) was mixed with CTAB (2.0 g) and deionized water (80.0 mL). The mixture was then sonicated for 20 min. The chloroform solvent was removed from the mixture at 70 °C. The aqueous CTAB-stabilized NCs dispersion was added into a mixture of deionized water (400.0 mL) and concentrated aqueous ammonia solution (2.5 mL). The mixture was homogenized for 30 min to form a uniform dispersion. TEOS (4.0 mL) was added drop wise into the dispersion with continuous stirring. After the reaction was allowed to proceed for 6 h, the product was separated with the help of a magnet and repeatedly washed with ethanol and water to remove nonmagnetic by-products. The resulting nanoparticles are referred to as 1-SPIO^{single}@SiO_2

2.3. Synthesis of clustered SPIO in a silica matrix (1-SPIO^{cluster}@SiO_2)

The core-shell 1-SPIO^{cluster}@SiO_2 nanoparticles were prepared by using Fe_3O_4 nanoparticle, synthesized in diethylene glycol. Fe_3O_4 particles (6.0 ± 1 nm in diameter) (0.1 g) was treated with 0.1 m aqueous HCl solution (25.0 mL) by ultrasonication for 10 min. The magnetite particles were separated and washed with deionized water and dispersed in a mixture containing CTAB (2.0 g) deionized water (480.0 mL), concentrated aqueous ammonia solution (2.5 mL) and ethanol (160.0 mL). The resulting mixture was homogenized for 0.5 h to obtain a uniform dispersion. TEOS (4.0 mL) was added drop wise into the dispersion with continuous stirring. After the reaction was allowed to proceed for 6 h, the product was separated with the help of a magnet and repeatedly washed with ethanol and water to remove nonmagnetic by-products. The resulting nanoparticles are referred to as 1-SPIO^{cluster}@SiO_2

2.4. Ligand synthesis: EDTA-bis(3-triethoxysilyl-*n*-propyl amide) (2)

EDTA-bis(anhydride) (0.512 g, 2 mmol) was dissolved in anhydrous pyridine (10 mL) under a steady flow of nitrogen using standard Schlenk line techniques. 3-Aminopropyl triethoxysilane (0.996 g, 4.5 mmol) was added into the solution of EDTA-bis(anhydride) and the resultant reaction mixture was magnetically stirred under nitrogen for 24 h. The product was then precipitated with copious amounts of hexane, isolated via centrifuge, washed with additional aliquots of hexanes and dried to yield (1.24 g, 90.6%) of the desired compound.

2.5. Surface modification of 1-SPIO^{single}@SiO_2 and 1-SPIO^{cluster}@SiO_2 with the ligand, EDTA-bis(3-triethoxysilyl-*n*-propyl amide)

1-SPIO^{single}@SiO_2 (or 1-SPIO^{cluster}@SiO_2) (0.05 g) was dispersed in a mixture of DMF (50.0 mL), anhydrous ethanol (30.0 mL) and concentrated aqueous ammonium hydroxide solution (1.0 mL). To this dispersion a solution of the ligand (0.1 g, 0.14 mmol) in DMF (3.0 mL) was added slowly and the mixture was stirred over night at 50 °C. The nanoparticles were separated by magnetic decantation using an external magnet and washed five times with EtOH in 20.0 mL portions. Finally, the purified nanoparticle was redispersed in acetone (60.0 mL) and refluxed for 6 h and decanted to remove the template CTAB in acetone. The extraction was repeated twice. The nanoparticles were then washed with deionized water and finally redispersed in PBS buffer (pH 7.2). The successful removal of CTAB was verified by fourier transform infrared (FT-IR) spectra analysis (Fig. S-1). The resulting nanoparticles are referred to as 2-SPIO^{single}@SiO_2 and 2-SPIO^{cluster}@SiO_2, respectively.

2.6. Surface modification of 1-SPIO^{single}@SiO_2 and 1-SPIO^{cluster}@SiO_2 with *N*-(trimethoxysilyl) propyl-*N*,*N*,*N*-trimethylammonium chloride and ligand

To obtain the nanocrystals with positively charged surface functionality, the same process was followed as described for 2-SPIO^{single}@SiO_2 and 2-SPIO^{cluster}@SiO_2, where after the ligand addition step the reaction mixture was stirred for 15 min followed by the addition of *N*-(trimethoxysilyl)propyl-*N*,*N*,*N*-trimethylammoniumchloride (0.1 mL). Subsequently the mixture was stirred at 50 °C overnight and purified as described above for 2-SPIO^{single}@SiO_2. The resulting nanoparticles are referred to as 3-SPIO^{single}@SiO_2 and 3-SPIO^{cluster}@SiO_2, respectively.

2.7. Cu^{2+} coordination with 2 & 3 SPIO^{single}@SiO_2 and 2&3 SPIO^{cluster}@SiO_2

A 0.01 m $Cu(OAc)_2$ solution in 0.1 m sodium acetate (3.0 mL) was mixed with the as-prepared 2-SPIO^{single}@SiO_2, 3-SPIO^{single}@SiO_2, 2-SPIO^{cluster}@SiO_2 and 3-SPIO^{cluster}@SiO_2 (10 mg) dispersion in 0.1 m sodium acetate in separate experiments and stirred at room temperature for 30 min. The nanoparticles coordinated with Cu^{2+} ions were magnetically confined from the solution by placing an external magnet next to the reaction vessel. After the supernatant solution was discarded, the nanoparticles were washed with deionized water (3 × 10 mL) to remove any non-coordinated Cu^{2+} ions.

2.8. Labeling adult stem cells with the contrast agents

The adult stem cells used in this study were obtained from the subcutaneous adipose tissue of five inbred male Lewis rats. Briefly, the isolated adipose tissue was washed extensively with

phosphate-buffered saline (PBS) to remove contaminating debris and blood cells. The adipose tissue was minced and digested with collagenase I (2 mg/mL Worthington Biochemical Corp, Lakewood, NJ) at 37 °C for 20–30 min. The digested adipose tissue was filtered twice with a 100-μm and then with a 25-μm nylon membrane to eliminate the undigested fragments. The cellular suspension was then centrifuged at 1000 rpm for 10 min. The cell pellets were re-suspended in cell-culture medium (CCM) and cultivated for 24 h at 37 °C in 5% CO_2. Unattached cells and debris were removed. The adherent ones were identified as stem cells and incubated for two days in a CCM containing 50 μg/mL of the synthesized SPIOs. Poly-l-lysine (2 μg/mL) was used as a transfecting reagent. Efficacy of SPIO labeling was assessed by measurement of the percent of the stem cells containing SPIO nanoparticles with Prussian blue staining. At two days after incubation in SPIO-containing CCM, most of the stem cells (>90%) were stained positive for SPIO particles.

2.9. Measurement of relaxivity

To determine the relaxivity of the four new types of SPIOs (2-$SPIO^{single}$@SiO_2, 3-$SPIO^{single}$@SiO_2, 2-$SPIO^{cluster}$@SiO_2 and 3-$SPIO^{cluster}$@SiO_2), they were dissolved in phosphate-buffered saline at a concentration of 120 μg/mL. To prevent precipitation of the SPIO nanoparticles, the SPIO-mediums was hardened by adding 0.1% agarose. A commercial MR contrast agent (Feridex®, Bayer, USA) was used as control.

The agarose gels were imaged on a 7 Tesla Bruker MR scanner (Bruker Inc, Karlsruhe, Germany) with a Helmholtz coil. Each image covered an 8 × 8 cm^2 field of view (FOV) with a 256 × 256 matrix, giving rise to a pixel size of 0.31 × 0.31 mm^2. T_2* relaxation times of the SPIO-containing agarose gels were measured using a gradient echo sequence with echo times (TE) of 4, 11, 18, and 25 m T_2 relaxation times of the agarose gels were measured using a spin-echo sequence with TE of 20 ms, 40 ms, 60 ms, 80 ms, 100 ms, 120 ms, 140 ms, 160 ms, and 180 ms. T_1 relaxation times of the gels were measured using an inversion-recovery (IR) spin-echo sequence with IR intervals of 12, 125, 500, 800, 1200, 1600, 2000, and 5000 m. Effect of the new SPIO nanoparticles on proton longitudinal relaxation time (T_1 relaxivity, r_1), transverse relaxation time (T_2 relaxivity, r_2 and T_2* relaxivity, r_2*) were calculated with the following function,

$$\text{relaxivity} = \left[\frac{1}{\text{Relaxation time}_{\text{SPIO}}} - \frac{1}{\text{Relaxation time}_{\text{no SPIO}}}\right] \div \text{concentration of SPIO}$$

3. Results and discussion

3.1. Crystal structure and morphology of the nanoparticles

There are many examples in the literature demonstrating different methods to produce stable water dispersions of superparamagnetic iron oxide nanoparticles (SPIOs) [15]. We have chosen to utilize a green synthesis approach developed by Caruntu et al. in which iron (II) and iron (III) salts are chelated to diethylene glycol and reduced at high temperature to produce highly crystalline, non-aggregated nanoparticles [14]. The powder X-ray diffractometry (XRD) of the as

synthesized SPIO could be indexed to the literature values of cubic crystalline bulk magnetite (Fe_3O_4) (JCPDS file No. 19-629) and no other secondary iron oxide phases could be traced. The PXRD data are presented in the supporting information (Fig. S-2). The refined lattice parameter derived from this PXRD data was 8.38 Å, which is essentially identical to that of the lattice parameter reported for the bulk Fe_3O_4 (8.396 Å) [16]. The size of the nanocrystals calculated using Scherrer's formula from the most intense peak of the XRD pattern was 5.5 ± 1 nm [17] which also agrees well with the average SPIO diameter calculated from the TEM images (6.0 ± 1 nm) (Fig. S-3). A major focus of this investigation is to elucidate how the clustering of nanoparticles will affect their ability to enhance MRI contrast as well as introducing different functional groups to the nanoparticle surface with different charges. One of the most effective ways to control both of these parameters is through the construction of a silica shell around the SPIOs.

The synthesis and modification of a silica shell around a nanoparticle core is a well studied and relatively simple procedure making it attractive as a scaffold to cover the SPIO as it will impart stability, biocompatibility and a surface that can be easily functionalized with a large variety of different ligands. Another promising attribute that silica provides is the ability to tune its porosity. In this report silica serves as a matrix to encapsulate either single or multiple SPIO as well as providing a high surface area for the introduction of desired functional groups. In addition, we have chosen to construct a porous silica shell which should allow water to penetrate into the silica matrix and interact with the SPIO nanoparticles at the interior of the nanoparticles and lead to better MRI contrast. As described in the experimental section, the synthesis of mesoporous silica shell was achieved by using cetyltrimethylammonium bromide as the templating agent as described by Liong et al. and Deng et al. [18] and [19]. As such, as the TEOS is being hydrolyzed and reacts with the SPIO nanoparticle surface, the presence of the CTAB micelles template the formation of a porous silica shell around the nanoparticle core. Interestingly we could tune the loading of SPIO within the silica matrix through a simple change in the starting nanoparticles. That is, when oleic acid-capped nanoparticles were employed in the synthesis of the MRI probes, a single iron oxide nanoparticle was encapsulated within the silica matrix. These nanoparticles are referred to as $SPIO^{single}@SiO_2$. Conversely, when the SPIO synthesized in the diethylene glycol were utilized in the development of the MRI probes, the resulting SPIO are clustered within the core of the nanoparticles. This architecture is referred to as $SPIO^{cluster}@SiO_2$. We speculate that the oleic acid stabilized SPIO produce $SPIO^{single}@SiO_2$ because the nanoparticles are made water soluble through the formation of a surfactant "double layer", where CTAB interdigitates with the oleic acid groups originally on the nanoparticle surface [20], [21] and [22]. The silica shell is then seeded around the existing CTAB and may not directly react with the surface of the SPIO nanoparticle. Conversely, in the case of the SPIOs synthesized in diethylene glycol, we believe that the hydrolyzed TEOS first reacts with the nanoparticle surface, displacing the chelated diethylene glycol which slightly destabilizes the SPIO. This destabilization leads to minor aggregation, resulting in the clustered core of the resulting $SPIO^{cluster}@SiO_2$ nanoparticles. The transmission electron microscope (TEM) images of 2-$SPIO^{single}@SiO_2$ and 2-$SPIO^{cluster}@SiO_2$ show that the nanoparticles appear essentially the same after surface modification and it is clear that there is a silica structure surrounding the SPIO nanocrystals at the center of the nanocomposites and there are many more nanoparticles encapsulated within the silica matrix for 2-$SPIO^{cluster}@SiO_2$ than for 2-$SPIO^{single}@SiO_2$ (Fig. 1). The resulting $SPIO^{single}@SiO_2$ and $SPIO^{cluster}@SiO_2$ provide an interesting model to elucidate

how the presence of the porous silica shell around single and cluster SPIO affects the T_2 weighted contrast of the nanoparticles in comparison to that of commercially available Feridex®.

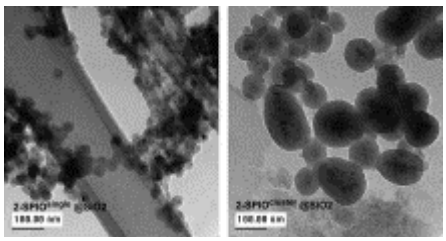

Fig. 1.

Representative TEM images of 2-SPIO^{single}@SiO_2 and 2-SPIO^{cluster}@SiO_2

There have been several reports highlighting that very simple functional groups on the surface of nanoparticles can lead to the rapid endocytosis of silica coated SPIOs [6]. We have developed a unique derivative of ethylenediaminetetraacetic acid (EDTA), which bears multiple negative charges. This EDTA-derivative which can be covalently bound to the surface of the SPIO@SiO_2, was obtained by condensing one equivalent of EDTA-bis(anhydride) with two equivalent of 3-aminopropyl triethoxysilane in dry pyridine at room temperature to generate EDTA-APTES (2) as described in the experimental section and shown in (Scheme 2). The resulting ligand was isolated as a moisture sensitive white solid and characterized by ^{1}H NMR and mass spectrometry (Figs. S-4 and 5).

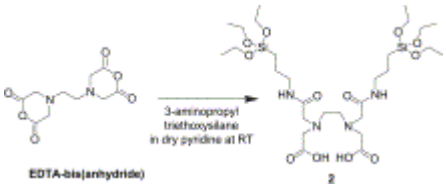

Scheme 2.

There are two hydrolyzable alkoxy silyl moieties present on the ligand allowing it to be covalently fixed to the surface of both SPIO@SiO_2 to give 2-SPIO^{single}@SiO_2 and 2-SPIO^{cluster}@SiO_2, respectively. This type of bimodal structure is well known to provide the stability of the surface functional group on silica. Another valuable feature of 2 is the six coordinating ligands are well known to form complex with Cu^{2+} ions with high thermodynamic stability, providing the opportunity to manipulate the surface charge on the nanoparticle through metal coordination. We can also potentially employ such ligand anchored nanoparticles as a

positron emission tomography (PET) agent after binding with ^{64}Cu. The coordination potential with Cu^{2+} by 2 on the silica surface of the nanocrystals was monitored by using UV–vis spectroscopy and XPS study (Figs. S-6 and 7). The Cu^{+2} coordination is also interesting because it essentially decreases the negative charge on the surface of the nanoparticles allowing one to study the influence of surface charge changes on cellular uptake. To study the effect of charge on the surface, we have also introduced a trimethylammonium-based ligand onto the surface of the nanoparticle to gain an understanding of how the presence of different charges affects the overall charges on the nanoparticle. A schematic representation of the different surface charges that our nanoparticles possess is presented in Scheme 1.

3.2. Zeta potential

The actual surface charge on each different nanoparticle, depicted in Scheme 1 was further investigated via zeta potential measurement at three different pH (Fig. 2). The zeta potential arises mainly from the presence of surface charges on the nanoparticles [23]. The positive zeta potential values at pH 4.2 for all the nanoparticles indicates positive surface of the nanoparticles at this pH. At lower pH the free amines of the ligands on the surface of the nanoparticles, 3-$SPIO^{cluster}@SiO_2$ and 2-$SPIO^{cluster}@SiO_2$ get protonated and along with the existing protonated carboxylate groups result into the positive surface. However, for 3-$SPIO^{cluster}@SiO_2$–Cu and 2-$SPIO^{cluster}@SiO_2$–Cu the coordination to Cu^{2+} by the amines and the carboxylates decreases the positive charge at the surface of the nanoparticles. The lower positive values of zeta potential for these nanoparticles indicate a lower positive charge density at their surface. The lower positive charge probably results from the protonation at the carbonyl oxygen atoms of coordinated carboxylate group or amide group. The higher positive zeta potential values of both 3-$SPIO^{cluster}@SiO_2$, 3-$SPIO^{cluster}@SiO_2$–Cu then 2-$SPIO^{cluster}@SiO_2$ and 2-$SPIO^{cluster}@SiO_2$–Cu are consistent with the presence of positively charged quaternary ammonium groups on the surface of these nanoparticles.

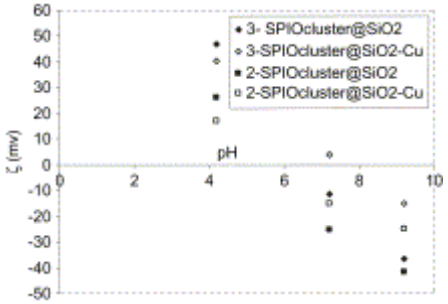

Fig. 2.

Plot of the zeta potential, ζ of the functionalized nanoparticles 2-$SPIO^{cluster}@SiO_2$ 3-$SPIO^{cluster}@SiO_2$, 2-$SPIO^{cluster}@SiO_2$–Cu and 3-$SPIO^{cluster}@SiO_2$–Cu as a function of the pH of the buffer solution.

At basic pH (7.2 and 9.2) the surfaces of the nanoparticles become negatively charged as reflected in the negative zeta potential values. In 3-SPIO^{cluster}@SiO_2 and 2-SPIO^{cluster}@SiO_2 the deprotonation of the carboxylic acid groups of the ligands leads to a negatively charged surface. The negative charge of the surface is partly neutralized by the coordination of the ligands to the Cu^{2+} ions. However, the negative zeta potential values of 3-SPIO^{cluster}@SiO_2–Cu and 2-SPIO^{cluster}@SiO_2–Cu, probably, arise from the negative charge of the leftover non-coordinated ligands. Further, the decrease of the zeta potential values for all the nanoparticles with increase in pH indicates higher degree of deprotonation at higher pH. The same trend also observes in case of 2-SPIO^{single}@SiO_2 and 3-SPIO^{single}@SiO_2 with and without copper (Fig. S 8)

Ultimately, these simple surface modification are attractive because they allows us to easily tune the surface charge on the nanoparticles with quite simple surface ligands and explore how these changes in surface charge affect both the endocytosis and the viability of the stem cells following SPIO@SiO_2 uptake. The cell viability study shows the nanopartilces prepared in this study do not negatively effect on viability of the ASC cells (Table S-2). However with these nanoparticles in hand, we were first interested in establishing how the relaxivites of the nanoparticles would compare to one another (*i.e.*, single nanoparticle *vs* clustered nanoparticle), and how the new nanoparticle architectures would compare to that of a commercially available SPIO-based MRI contrast agent, namely Feridex®.

3.3. Relaxivity

To estimate the potential of the different SPIO@SiO_2 architectures as MRI contrast agents, the relaxivities of the nanocrystals were determined through the dispersion of the nanoparticles in 0.1% agarose gel. The relaxivity data of the silica-coated nanocrystals and Feridex® are presented in Fig. 2 for comparison. The SPIO is a well known T_2 based contrast agent that exhibits r_2 values significantly higher in comparison to the r_1 values. When equal concentrations (with respect to the total iron oxide concentration) of 2-SPIO^{single}@SiO_2, 3-SPIO^{single}@SiO_2, 2-SPIO^{cluster}@SiO_2 and 3-SPIO^{cluster}@SiO_2 were incorporated into the agarose gel in separate experiments it is evident that the clustered nanoparticles provide a significantly enhanced relaxivity in comparison to that of the nanoparticles containing single SPIOs (Fig. 3). This is particularly impressive considering that the actual number of 2 & 3-SPIO^{cluster}@SiO_2 in the sample will be significantly smaller than that for the 2 & 3-SPIO^{single}@SiO_2 because a similar concentration of iron oxide was used in the analysis, but there are many more SPIO in the core of the clustered nanoparticles. We were surprised to see that the presence of the porous silica shell does not appear to provide a significant advantage over the dextran shell on the Feridex® nanoparticles. In fact, the silica shell appears to dampen the relaxivity observed for the 2- and 3-SPIO^{single}@SiO_2 nanoparticles (r_2 = 3.9 and 3.0 $S^{-1}mM^{-1}$respectively) in comparison to that for Feridex®. Only when the SPIO are clustered within the silica matrix the relaxivity values increase to match that of the Feridex® (Fig. 3) (r_2 = 9.0 & 7.6 $S^{-1}mM^{-1}$).

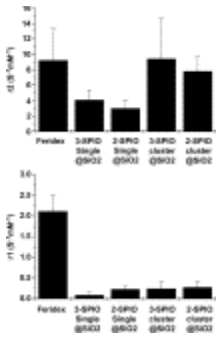

Fig. 3.

Comparison of r_1 and r_2 values of the 2-SPIO^{single}@SiO_2, 3-SPIO^{single}@SiO_2 2-SPIO^{cluster}@SiO_2, 3-SPIO^{cluster}@SiO_2 nanocrystals and Feridex®.

The trends in the relaxivity values are reflected in the phantom images obtained with 2-SPIO^{single}@SiO_2, 2-SPIO^{cluster}@SiO_2, 3-SPIO^{single}@SiO_2 and 3-SPIO^{cluster}@SiO_2 acquired using 120 μg/mL nanocrystals in 0.1% agarose gel (Fig. 4) in separate experiments. The phantom images clearly show that the T_2 images obtained with the nanocrystals of both 2-SPIO^{cluster}@SiO_2 and 3-SPIO^{cluster}@SiO_2 exhibit better contrast compared to the same for 2-SPIO^{single}@SiO_2 and 3-SPIO^{single}@SiO_2. 2-SPIO^{cluster}@SiO_2 and 3-SPIO^{cluster}@SiO_2 are comparable to Feridex®.

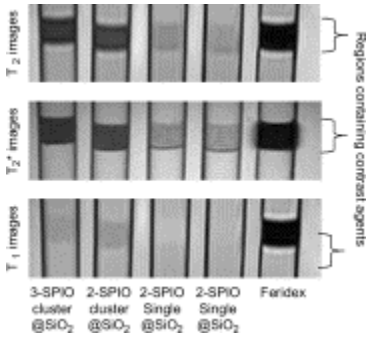

Fig. 4.

The phantom images of nanoparticles embedded in 0.1% agarose gel.

Analysis of these data again suggests that the T_2 relaxivity is increased dramatically with SPIO clustering inside of the silica matrix. For example, the effect of SPIO clustering on the phantom MRI images in (Fig. 4) show that both 2-SPIO^{cluster}@SiO_2 and 3-SPIO^{cluster}@SiO_2 show a significantly darker T_2-weighted image than those for 2-SPIO^{single}@SiO_2 and 3-SPIO^{single}@SiO_2.

The SPIO^{cluster}@SiO_2 nanoparticle appear to be better candidates for use as MRI contrast agents; however, if they are to be truly useful in stem cell tracking it is necessary to investigate how surface charge of the nanoparticle affects their ability to be endocytosed by the stem cells and if cells remain viable following the nanoparticle uptake.

3.4. Cell labeling; iron uptake by rat adult stem cells

Cellular uptake of nanoparticles was studied with rat adult stem cells (ASCs). The ASCs were incubated in a cell-culture medium containing 2-SPIO^{cluster}@SiO_2, 3-SPIO^{cluster}@SiO_2 and Feridex® independently for two days and then stained with Prussian blue to identify the cellular uptake. Poly-l-lysine (PLL) was used to aid on the iron-transfection into the cells.

The staining results suggest that the extent of intracellular labeling for the mixed charge nanoparticles (3-SPIO^{cluster}@SiO_2) is similar to that of Feridex®, while the negatively charged nanocrystals (2-SPIO^{cluster}@SiO_2) are less effective at labeling the stem cells than Feridex® (Fig. 5) despite the fact PLL was used to aid on nanoparticle uptake. Previously it has been reported that modified iron oxide nanocrystals with a cationic surface have a better cell-labeling efficiency than the same with a negatively charged and neutral nanoparticles [24].

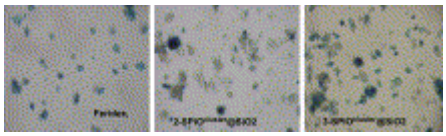

Fig. 5.

Microscopic observation of ACS cell labeled with nanpaprticle and Feridex®.

The following figure (Fig. 6) depicts the cell-labeling efficiency of Cu^{2+} bound nanocrystals 2-SPIO^{cluster}@SiO_2 and 3-SPIO^{cluster}@SiO_2 when rat ASCs were labeled independently with both the types of nanocrystals and Feridex®. The cells were also stained with protamine sulfate (to stain the SPIO for enhance visualization) for 72 h. Interestingly, when copper is coordinated to the surface of the nanoparticles, we have demonstrated that the coordination of the negatively charged carboxylate groups would no longer remain free resulting in significant change in surface charges. Upon Cu^{2+} binding, the surface charges on 2-SPIO^{cluster}@SiO_2 and 3-SPIO^{cluster}@SiO_2 become less negative and essentially neutral respectively. The result of this surface charge changes enhanced cellular uptakes of these nanoparticles have been observed at low concentration as demonstrated in (Fig. 6).

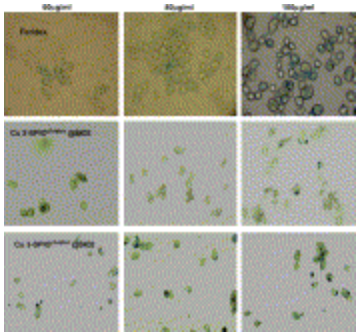

Fig. 6.

Microscopic observation of ACS cell labeled with Copper bonded nanpaprticle and Feridex®.

Though the presence of Cu^{2+} on the surface of nanoparticles does improve the endocytosis of the nanoparticles in the ASC cells, it unfortunately also significantly dampen the r_2 values and the nanoparticles no longer act as good T_2 contrast agents following copper coordination (Fig. S-9). It is interesting, however, that the superparamagnetic iron-oxide nanoparticles are currently used in the clinic for MR imaging of the hepatobiliary system, presumably because the nanoparticles of this size are readily taken into the endoreticular system and delivered to the liver [5], [25], [26] and [27]. This is intriguing because there is a rare and difficult to detect disease, the Wilson's disease, which causes excess copper ion storage in the liver and high copper ion concentration in the urine. This is of interest because it could be possible to monitor the levels of copper ions in the liver or urine based on the strength of the MRI contrast. That is a strong decrease in the T_2 contrast in comparison to a control sample could potentially signal the presence of high concentrations of copper ions and indicate a patient may have Wilson's disease [28]. Currently the detection of Wilson's disease requires a liver tissue sample to be extracted from the patient, so an MRI-based procedure capable of signaling elevated levels of copper ions, particularly in the liver, is quite attractive as it would be significantly less invasive.

4. Conclusions

In summary, we have designed a series of multifunctional iron oxide encapsulated mesoporous silica nanoparticles with tunable surface charges that can modulate the ability for stem cells to endocytose them. The resulting nanoparticle probe with clustered iron oxide cores display relaxivities comparable to commercially available Feridex® and can potentially serve as MRI or PET contrast agents. The nanoparticles demonstrate excellent biocompatibility, exhibiting no short-term cytotoxicity to the ASC cells and high cell uptake efficiency. These properties provide potential for these nanoparticles in stem cell tracking and may even provide an alternative strategy for the detection of Wilson's disease.

References

[1] J.S. Choi, J.C. Park, H. Nah, S. Woo, J. Oh and M. Kim *et al.*, A hybrid nanoparticle probe for dual-Modality positron emission tomography and magnetic resonance imaging, *Angew Chem Int Ed* **47** (2008), pp. 6259–6262.

[2] K. Toth, L. Helm and A.E. Merbach, The chemistry of contrast agents in medical magnetic resonance imaging, Wiley, Chichester (2001).

[3] P. Caravan, J.J. Ellison, T.J. McMurry and R.B. Lauffer, Gadolinium(III)chelates as MRI contrast agents: structure, dynamics and applications, *Chem Rev* **99** (1999), pp. 2293–2352.

[4] K.N. Raymond and V.C. Pierre, Next generation, high relaxivity gadolinium MRI agents, *Bioconjug Chem* **16** (2005), pp. 3–8.

[5] J.H. Lee, Y.M. Huh, Y.W. Jun, J.W. Seo, T.J. Jung and H.T. Song *et al.*, Artificially engineered magnetic nanoparticles for ultra-sensitive molecular imaging, *Nat Med* **13** (2007), pp. 95–99.

[6] T.H. Chung, S.H. Wu, M. Yao, C.W. Lu, Y.S. Lin and Y. Hung *et al.*, The effect of surface charge on the uptake and biological function of mesoporous silica nanoparticles in 3T3-L1 cells and human mesenchymal stem cells, *Biomaterials* **28** (2007), pp. 2959–2966.

[7] C. Catana, Y.B. Wu, M.S. Judenhofer, J.Y. Qi, B.J. Pichler and S.R. Cherry, Simultaneous acquisition of multislice PET and MR images: initial results with a MR-compatible PET scanner, *J Nucl Med* **47** (2006), pp. 1968–1976.

[8] S.R. Cherry, The 2006 Henry N. Wagner lecture: of mice and men (and Positrons) advances in PET imaging technology, *J Nucl Med* **47** (2006), pp. 1735–1745.

[9] S.R. Cherry, Fundamentals of positron emission tomography and applications in preclinical drug development, *J Clin Pharmacol* **41** (2001), pp. 482–491.

[10] Lee HaY, Z. Li, K. Chen, A.R. Hsu, Xu Ch and J. Xie *et al.*, PET/MRI dual-modality tumor imaging using arginine-glycine-aspartic (RGD)–conjugated radiolabeled iron oxide nanoparticles, *J Nucl Med* **49** (2008), pp. 1371–1379.

[11] C.P. Tsai, Y. Hung, Chou YiH, D.M. Huang, J.K. Hsiao and C. Chang *et al.*, High-contrast paramagnetic fluorescent mesoporous silica nanorods as a multifunctional cell-imaging probe, *Small* **4** (2) (2008), pp. 186–191.

[12] J. Kim, J.E. Lee, S.H. Lee, J.H. Yu, J.H. Lee and T.G. Park *et al.*, Designed fabrication of a multifunctional polymer nanomedical platform for simultaneous cancer-targeted imaging and magnetically guided drug delivery, *Adv Mater* **20** (2008), pp. 478–483.

[13] H. Ai, C. Flask, B. Weinberg, X. Shuai, M.D. Pagel and D. Farrell *et al.*, Magnetite-loaded polymeric micelles as ultrasensitive magnetic-resonance probes, *Adv Mater* **17** (2005), pp. 1949–1952.

[14] D. Caruntu, G. Caruntu, Y. Chen, C.J. O'Connor, G. Goloverda and V.L. Kolesnichenko, Synthesis of variable-sized nanocrystals of Fe_3O_4 with high surface reactivity, *Chem Mater* **16** (2004), pp. 5527–5534.

[15] S. Laurent, D. Forge, M. Port, A. Roch, C. Robic and L.V. Elst *et al.*, Magnetic iron oxide nanoparticles: synthesis, stabilization, vectorization, physicochemical characterizations, and biological applications, *Chem Rev* **108** (2008), pp. 2064–2110.

[16] R.M. Cornell and U. Schwertmann, The iron oxides: structure, properties, reactions, occurrence and uses, VCH, New York (1996) pp. 28.

[17] A.R. West, Solid state chemistry and its applications, John Wiley & Sons, London (1984) pp. 174.

[18] M. Liong, J. Lu, M. Kovochich, T. Xia, S.G. Ruehm and A.E. Nel *et al.*, Multifunctional inorganic nanoparticles for imaging, targeting, and drug delivery, *Acs Nano* **2** (2008), pp. 889–896.

[19] Y. Deng, D. Qi, C. Deng, X. Zhang and D. Zhao, Superparamagnetic high-magnetization microspheres with an Fe_3O_4@SiO_2 core and perpendicularly aligned mesoporous SiO_2 shell for removal of microcystins, *J Am Chem Soc* **130** (2008), pp. 28–29.

[20] H. Fan, K. Yang, D.M. Boye, T. Sigmon, K.J. Malloy and H. Xu *et al.*, Self-assembly of ordered, robust, three-dimensional gold nanocrystal/silica arrays, *Science* **304** (2004), pp. 567–571.

[21] J. Kim, Lee JiE, J. Lee, J.H. Yu, B.C. Kim and K. An *et al.*, Magnetic fluorescent delivery vehicle using uniform mesoporous silica spheres embedded with monodisperse magnetic and semiconductor nanocrystals, *J Am Chem Soc* **128** (2006), pp. 688–689.

[22] J. Kim, H.S. Kim, N. Lee, T. Kim, H. Kim and T. Yu *et al.*, Multifunctional uniform nanoparticles composed of a magnetite nanocrystal core and a mesoporous silica shell for magnetic resonance and fluorescence imaging and for drug delivery, *Angew Chem Int Ed* **47** (2008), pp. 8438–8442.

[23] V. Mahalingam, S. Onclin, M. Péter, B. Ravoo, J. Huskens and D.N. Reinhoudt, Directed self-assembly of functionalized silica nanoparticles on molecular printboards through multivalent supramolecular interactions, *Langmuir* **20** (2004), pp. 11756–11762.

[24] H.T. Song, J.S. Choi, Y.M. Huh, S. Kim, Y.W. Jun and J.S. Suh *et al.*, Surface modulation of magnetic nanocrystals in the development of highly efficient magnetic resonance probes for intracellular labeling, *J Am Chem Soc* **127** (2005), pp. 9992–9993.

[25] Y. Jun, Y.M. Huh, J. Choi, J.H. Lee, H.T. Song and S. Kim *et al.*, Nanoscale size effect of magnetic nanocrystals and their utilization for cancer diagnosis via magnetic resonance imaging, *J Am Chem Soc* **127** (2005), pp. 5732–5733.

[26] Y.J. Huh, H.T. Song, S. Kim, J. Choi, J.H. Lee and S. Yoon, In vivo magnetic resonance detection of cancer by using multifunctional magnetic nanocrystals, *J Am Chem Soc* **127** (2005), pp. 12387–12391.

[27] A.S. Arbab, W. Liu and J.A. Frank, Cellular magnetic resonance imaging: current status and future prospects, *Exp Rev Med Dev* **3** (2006), pp. 427–439.

[28] M.L. Schilsky, Wilson disease: current status and the future, *Biochimie* **1** (2009), pp. 1278–1281.

Appendix. Supplementary data

Appendix.

Figures with essential colour discrimination. Fig. 5 and Fig. 6 and Scheme 1 of this article may be difficult to interpret in black and white. The full colour images can be found in the online version, at doi:10.1016/j.biomaterials.2009.12.025.